Tsunami and acoustic-gravity waves in water of constant depth

Gali Hendin and Michael Stiassnie

Citation: Physics of Fluids (1994-present) **25**, 086103 (2013); doi: 10.1063/1.4817996
View online: http://dx.doi.org/10.1063/1.4817996
View Table of Contents: http://scitation.aip.org/content/aip/journal/pof2/25/8?ver=pdfcov
Published by the AIP Publishing

PHYSICS OF FLUIDS **25**, 086103 (2013)

Tsunami and acoustic-gravity waves in water of constant depth

Gali Hendin and Michael Stiassnie
Faculty of Civil and Environmental Engineering, Technion – Israel institute of technology, Haifa 32000, Israel

(Received 11 February 2013; accepted 27 July 2013; published online 19 August 2013)

A study of wave radiation by a rather general bottom displacement, in a compressible ocean of otherwise constant depth, is carried out within the framework of a three-dimensional linear theory. Simple analytic expressions for the flow field, at large distance from the disturbance, are derived. Realistic numerical examples indicate that the Acoustic-Gravity waves, which significantly precede the Tsunami, are expected to leave a measurable signature on bottom-pressure records that should be considered for early detection of Tsunami. © *2013 AIP Publishing LLC*. [http://dx.doi.org/10.1063/1.4817996]

I. INTRODUCTION

In a series of recent studies, the Russian group lead by Professor M. A. Nosov has demonstrated the importance of the small compressibility of the ocean in the process of Tsunami generation; see Nosov[1,2] and Nosov *et al.*[3–5] These studies follow the foundation laid in earlier attempts by Miyoshi,[6] Sells,[7] and Yamamoto.[8]

The overwhelming majority of ocean-wave studies ignores the minute compressibility of the water, which is expected to have, and in most cases has, only a negligible effect on the main physical processes. However, a rather straightforward analysis of the linearized problem in water of constant depth reveals that for any wave period (T) smaller than four times the water depth (h) to the speed of sound (c) ratio (i.e., $T < 4h/c$), two or more propagating modes are possible.

This state-of-affairs is rather different from the situation in an incompressible ocean, for which only one propagating mode exists. In the balance of this paper, we shell refer to these modes by their wave numbers: $q_0 > 2\pi/cT > q_1 > q_2 > \ldots > q_N$; where q_0 represents the mode which also exists in a incompressible ocean, and will be called the Tsunami mode, whereas $q_1, q_2, \ldots, q_N$ represent the additional propagating modes, which result from taking the compressibility of water into account, and will be called the Acoustic-Gravity modes. A disturbance at the ocean floor, such as that caused by a submarine earthquake, produces many different modes. Most of these modes ($q_{N+1}, q_{N+2} \ldots$) are non-propagating (evanescent) and of local importance only. However, the Tsunami q_0 and the leading Acoustic-Gravity mode q_1 (and of less importance also $q_2, \ldots, q_N$) propagate away from the earthquake site and travel to a great distance. An Acoustic-Gravity wave travels significantly faster than the Tsunami, and thus, is a possible candidate for an early warning about the approach of the latter.

This paper is an extension to three dimensions and a generalization to arbitrary bottom motions of the work in Stiassnie.[9] Stiassnie[9] provided results for an infinitely long stripe shaped disturbance, whereas here we give an analytic solution for the general problem and detailed calculations for piston type motions of circular and rectangular disturbances.

II. FORMULATION

Let us consider a layer of an ideal compressible homogenous fluid of constant depth h in the field of gravity, and assume it is unbounded in the horizontal (x, y) plane. The origin of the coordinate system $oxyz$ is at the unperturbed free-surface, and the z-axis is oriented upwards. In order to find

the wave disturbance $z = \eta(x, y, t)$, that is, excited at the fluid surface by a bottom motion $z = -h + \zeta(x, y, t)$, it is necessary to solve for the flow velocity potential $\Phi(x, y, z, t)$ which is governed by the wave equation

$$\nabla^2 \Phi = \frac{1}{c^2} \Phi_{tt}, \quad -h \le z \le 0, \tag{1}$$

and the linear free-surface and bottom boundary conditions

$$\Phi_{tt} + g\Phi_z = 0, \quad z = 0, \tag{2}$$

$$\Phi_z = \zeta_t, \quad z = -h, \tag{3}$$

where $c = 1500$ m/s is the speed of sound in the water and $g = 9.81$ m/s^2 is the acceleration due to gravity. Note that outside the area of the motion ζ, the bottom is assumed to be horizontal and rigid.

The free-surface elevation and the dynamic bottom pressure are given by

$$\eta = -\frac{1}{g} \Phi_t, \quad z = 0, \tag{4}$$

$$p_b = -\rho \Phi_t, \quad z = -h, \tag{5}$$

where $\rho = 1000$ kg/m^3 is the water density.

In Sec. III we present the result for a circular disturbance with radius R, which rises at constant speed w_0 during the time interval $(0, \tau)$ and stops at $z = -h + w_0\tau$. For such a disturbance,

$$\zeta_t = w_0 H\left(R^2 - x^2 - y^2\right) H\left(t\left(\tau - t\right)\right), \tag{6}$$

where H is the Heaviside function.

In Sec. IV we apply the limits for $R, \tau \to 0$, on the solution of Sec. III and divide the result by $w_0 \pi R^2 \tau$ to obtain a Green function and its stationary-phase approximation. The results for circular and rectangular disturbances are presented in Secs. V and VI, respectively. Some general discussion about the inverse problem is given in Sec. VII. Some technical mathematical and numerical details are given in Appendices A–C.

III. SOLUTION FOR A CIRCULAR DISTURBANCE

The $t \to \omega$ Fourier transform of the velocity potential is defined by

$$f(x, y, z, \omega) = \frac{1}{\sqrt{2\pi}} \int_{-\infty}^{\infty} \Phi(x, y, z, t) \cdot e^{-i\omega t} \cdot dt. \tag{7}$$

Substituting (6) in (3) and taking the Fourier transform of (1)–(3) yields

$$\nabla^2 f = -\frac{\omega^2}{c^2} f, \quad -h \le z \le 0, \tag{8}$$

$$f_z - \frac{\omega^2}{c^2} f = 0, \quad z = 0, \tag{9}$$

$$f_z = \zeta_0(\omega) H\left(R^2 - x^2 - y^2\right), \quad z = -h, \tag{10a}$$

where

$$\zeta_0 = \frac{i w_0}{\sqrt{2\pi}} \cdot \frac{e^{-i\omega\tau} - 1}{\omega}. \tag{10b}$$

Switching to cylindrical coordinates (r, θ, z), defining two regions: an inner region $r < R$ and an outer region $r > R$, using the method of separation of variables, applying a boundness condition on the inner solution and Somerfield's radiation condition on the outer region, matching the inner

solution and its r derivative to their counterparts for the outer potential at $r = R$, and applying the inverse Fourier transform gives

for $r < R$

$$\Phi_{in}(r,z,t) =$$

$$-4w_0R\int_0^\infty \frac{\mu_0\cosh[\mu_0(z+h)]\sin\left(\frac{\omega\tau}{2}\right)}{\omega q_0[\sinh(2\mu_0h)+2\mu_0h]}\cdot\left[J_1(q_0R)\sin\left(\omega t-\frac{\omega\tau}{2}\right)-Y_1(q_0R)\cos\left(\omega t-\frac{\omega\tau}{2}\right)\right]$$

$$\cdot J_0(q_0r)\,d\omega$$

$$-4w_0R\sum_{n=1}^\infty\int_{\omega_{sn}}^\infty \frac{\mu_n\cos[\mu_n(z+h)]\sin\left(\frac{\omega\tau}{2}\right)}{\omega q_n[\sin(2\mu_nh)+2\mu_nh]}\cdot\left[J_1(q_nR)\sin\left(\omega t-\frac{\omega\tau}{2}\right)-Y_1(q_nR)\cos\left(\omega t-\frac{\omega\tau}{2}\right)\right]$$

$$\cdot J_0(q_nr)\,d\omega$$

$$+\frac{8Rw_0}{\pi}\sum_{n=1}^\infty\int_0^{\omega_{sn}}\frac{\mu_n\cos[\mu_n(z+h)]\sin\left(\frac{\omega\tau}{2}\right)}{\omega q_n[\sin(2\mu_nh)+2\mu_nh]}\cdot\cos\left(\omega t-\frac{\omega\tau}{2}\right)\cdot K_1(q_nR)\cdot I_0(q_nr)d\omega$$

$$+\frac{2w_0}{\pi}\int_0^\infty\cos\left(\omega t-\frac{\omega\tau}{2}\right)\sin\left(\frac{\omega\tau}{2}\right)\cdot\frac{c}{\omega^2}\cdot\frac{\omega c\cdot\sin\left(\frac{\omega}{c}z\right)+g\cdot\cos\left(\frac{\omega}{c}z\right)}{g\cdot\sin\left(\frac{\omega}{c}h\right)+\omega c\cdot\cos\left(\frac{\omega}{c}h\right)}d\omega, \tag{11a}$$

and for $r > R$

$$\Phi_{out}(r,z,t) =$$

$$-4Rw_0\int_0^\infty\frac{\mu_0\cosh[\mu_0(z+h)]\sin\left(\frac{\omega\tau}{2}\right)}{\omega q_0[\sinh(2\mu_0h)+2\mu_0h]}\cdot J_1(q_0R)\cdot\left[J_0(q_0r)\sin\left(\omega t-\frac{\omega\tau}{2}\right)\right.$$

$$\left.-Y_0(q_0r)\cos\left(\omega t-\frac{\omega\tau}{2}\right)\right]d\omega$$

$$-4Rw_0\sum_{n=1}^\infty\int_{\omega_{sn}}^\infty\frac{\mu_n\cos[\mu_n(z+h)]\sin\left(\frac{\omega\tau}{2}\right)}{\omega q_n[\sin(2\mu_nh)+2\mu_nh]}\cdot J_1(q_nR)\cdot\left[J_0(q_nr)\sin\left(\omega t-\frac{\omega\tau}{2}\right)\right.$$

$$\left.-Y_0(q_nr)\cos\left(\omega t-\frac{\omega\tau}{2}\right)\right]d\omega$$

$$-\frac{8Rw_0}{\pi}\sum_{n=1}^\infty\int_0^{\omega_{sn}}\frac{\mu_n\cos[\mu_n(z+h)]\sin\left(\frac{\omega\tau}{2}\right)}{\omega q_n[\sin(2\mu_nh)+2\mu_nh]}\cdot\cos\left(\omega t-\frac{\omega\tau}{2}\right)\cdot I_1(q_nR)\cdot K_0(q_nr)d\omega. \tag{11b}$$

In (11a) and (11b) J, Y are Bessel functions of the first and second kind, and I, K are modified Bessel functions of the first and second kind.

The Eigenvalues $\mu = \mu_0$ and $\mu = i\mu_n$, $n = 1, 2, \ldots$ (where all μ_0, μ_n are real and positive) are solutions of the dispersion equation:

$$\mu\cdot\tanh(\mu h) = \frac{\omega^2}{g} \tag{12}$$

and

$$q_0 = \left(\mu_0^2+\frac{\omega^2}{c^2}\right)^{1/2}, \tag{13a}$$

$$q_n = \left(\frac{\omega^2}{c^2}-\mu_n^2\right)^{1/2}, \quad \omega\geq\omega_{sn}, \tag{13b}$$

$$q_n = \left(\mu_n^2 - \frac{\omega^2}{c^2}\right)^{1/2}, \quad \omega \le \omega_{sn}, \tag{13c}$$

where ω_{sn} are given by the roots of

$$\mu_n(\omega_{sn}) = \frac{\omega_{sn}}{c}, \quad n = 1, 2, \ldots . \tag{14}$$

Good approximated solutions of (12) and (14) are

$$\omega_{sn} = (2n-1)\frac{\pi c}{2h}, \quad n = 1, 2, \ldots . \tag{15}$$

In (11b) the first, second, and third lines represent the Tsunami, the Acoustic-Gravity waves, and the evanescent modes, respectively. For further details about the mathematical procedure, see Appendix B, as well as Hendin.[10]

IV. SOLUTION FOR A GENERAL DISTURBANCE

Taking the outer region solution (11b), letting $R, \tau \to 0$, and dividing by $w_0 \pi R^2 \tau$ gives

$$G(r,z,t) = \int_0^\infty \frac{\mu_0 \cosh[\mu_0(z+h)]}{\pi[\sinh(2\mu_0 h) + 2\mu_0 h]} \cdot [Y_0(q_0 r)\cos(\omega t) - J_0(q_0 r)\sin(\omega t)]d\omega$$

$$+\sum_{n=1}^\infty \int_{\omega_{sn}}^\infty \frac{\mu_n \cos[\mu_n(z+h)]}{\pi[\sin(2\mu_n h) + 2\mu_n h]} \cdot J_1(q_n R) \cdot [Y_0(q_n r)\cos(\omega t) - J_0(q_n r)\sin(\omega t) -]d\omega$$

$$-2\sum_{n=1}^\infty \int_0^{\omega_{sn}} \frac{\mu_n \cos[\mu_n(z+h)]}{\pi^2[\sin(2\mu_n h) + 2\mu_n h]} \cdot K_0(q_n r) \cdot \cos(\omega t)d\omega. \tag{16}$$

In terms of the above Green function the outer solution for a general disturbance is given by

$$\Phi(x,y,z,t) = \int_{-\infty}^\infty \int_{-\infty}^\infty \int \zeta_t(X,Y,T) \cdot G\left(\sqrt{(x-X)^2 + (y-Y)^2}, z, (t-T)\right) dXdYdT. \tag{17}$$

For large distances, i.e., $r \to \infty$, one can use the following asymptotic expansion of the Bessel functions:

$$J_0(qr) = \sqrt{\frac{2}{\pi qr}} \cdot \cos\left(qr - \frac{\pi}{4}\right), \tag{18a}$$

$$Y_0(qr) = \sqrt{\frac{2}{\pi qr}} \cdot \sin\left(qr - \frac{\pi}{4}\right), \tag{18b}$$

$$K_0(qr) = \frac{e^{-qr}}{\sqrt{2\pi qr}}, \tag{18c}$$

and simplify (16) for $r \gg h$:

$$G_1(r,z,t) = \sqrt{\frac{2}{\pi^3 r}} \cdot \int_0^\infty \frac{\mu_0 \cosh[\mu_0(z+h)]}{q_0^{1/2}[\sinh(2\mu_0 h) + 2\mu_0 h]} \cdot \sin\left(q_0 r - \omega t - \frac{\pi}{4}\right)d\omega$$

$$+\sqrt{\frac{2}{\pi^3 r}} \cdot \sum_{n=1}^\infty \int_{\omega_{sn}}^\infty \frac{\mu_n \cos[\mu_n(z+h)]}{q_n^{1/2}[\sin(2\mu_n h) + 2\mu_n h]} \cdot \sin\left(q_n r - \omega t - \frac{\pi}{4}\right)d\omega. \tag{19}$$

The oscillation in time of the integrands for the Acoustic-Gravity waves (second line in (19)) is much faster than that of the Tsunami (first line in (19)), and causes substantial difficulties when one tries to apply standard Quadrature routines. However, the Green function $G_1(r, z, t)$ can be further simplified by applying the Stationary-Phase method to the second line, which will limit its validity to $t > r/c$. Note that the stationary points and the appropriate wave numbers are given by

$$\hat{\omega}_n = \frac{\alpha_n c}{h\sqrt{\left[1-(r/ct)^2\right]}}, \tag{20a}$$

$$\hat{q}_n = \frac{\alpha_n (r/ct)}{h\sqrt{\left[1-(r/ct)^2\right]}}, \tag{20b}$$

where

$$\alpha_n = (2n-1)\frac{\pi}{2}, \qquad n = 1, 2, \ldots . \tag{20c}$$

Following Carrier *et al.*, Ref. 11 Sec. 6-4, we obtain for $r/h \gg 1$ and $t > r/c$

$$G_2(r, z, t) = \sqrt{\frac{2}{\pi^3 r}} \cdot \int_0^\infty \frac{\mu_0 \cosh\left[\mu_0 (z+h)\right]}{q_0^{1/2}\left[\sinh(2\mu_0 h) + 2\mu_0 h\right]} \cdot \sin\left(q_0 r - \omega t - \frac{\pi}{4}\right) d\omega$$

$$-\frac{c}{\pi r h} \cdot \frac{1}{\sqrt{(ct/r)^2 - 1}} \cdot \sum_{n=1}^{\infty} \cos\left[\hat{\mu}_n (1 + z/h)\right] \cdot \cos\left(\hat{q}_n r - \hat{\omega}_n t\right), \tag{21a}$$

where

$$\hat{\mu}_n = \frac{\alpha_n}{h}\left(1 + \frac{g}{h\hat{\omega}_n^2}\right). \tag{21b}$$

V. RESULTS FOR A CIRCULAR DISTURBANCE

In all our calculations here, and elsewhere in this paper, we take 10 Acoustic-Gravity modes. This choice was demonstrated to be adequate in Stiassnie.[9]

A. Comparison with previous work

Nosov[2] uses a Hankel transform in space r, and a Laplace transform in time t, to obtain an analytical solution equivalent to (11a) and (11b). We believe that our expressions are not only physically more transparent but also easier in their numerical realization. In Figure 1 we display our results for the free surface elevation $\eta(r = 0, t)$ of a circular disturbance with the same input parameters that were used by Nosov[2]: $h = 3.6$ km, $R = 36$ km, and $\tau = 12$ s. This figure should be compared with Figure 2(a) in Nosov.[2] The agreement between both calculations is satisfactory, for the Tsunami (given by the dashed line) as well as for the Acoustic-Gravity wave superposed on the Tsunami (given by the solid line).

In Tsunami calculations it is quite often assumed that the initial free-surface elevation is very similar to the initial rise of the ground, see Tobias and Stiassnie.[12] This assumption is strengthened by the results in Figure 2, where we present $\eta(r, t)$, for $r \le R$ and $t = \tau$, $t = 10\tau$, and $t = 100\tau$. Note that at $t = \tau$ the free-surface elevation is almost constant and equal to $w_0\tau$. From this figure one can also see that the surface elevation amplitudes of the Acoustic-Gravity waves are much smaller than that of the Tsunami.

It is important to note that the development of the Tsunami wave is almost insensitive to the rising time of the bottom, τ; in contrast to the strong dependence of the Acoustic-Gravity waves on this parameter. From Figure 1 one can see that the dominant wave-period of the Acoustic-Gravity waves is roughly τ. Moreover, no propagating Acoustic-Gravity waves will exist for τ larger than about $4h/c$.

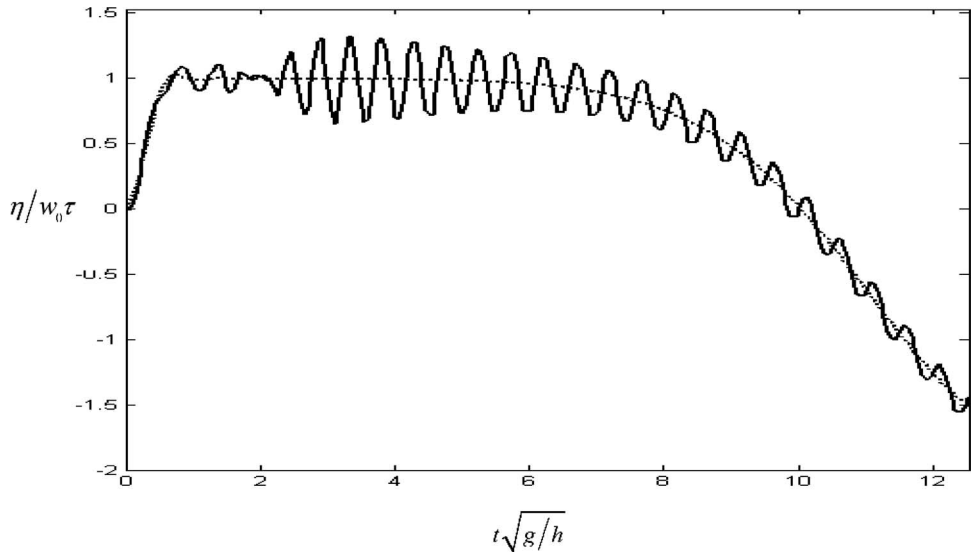

FIG. 1. The free surface elevation at the origin, originated by a circular disturbance, for comparison with Nosov (2000). $\eta(t)$ at observation point $r = 0$ for depth $h = 3.6$ km, radius $R = 36$ km, and duration $\tau = 12$ s. Acoustic-Gravity + Tsunami (solid line), Tsunami only (dashed line).

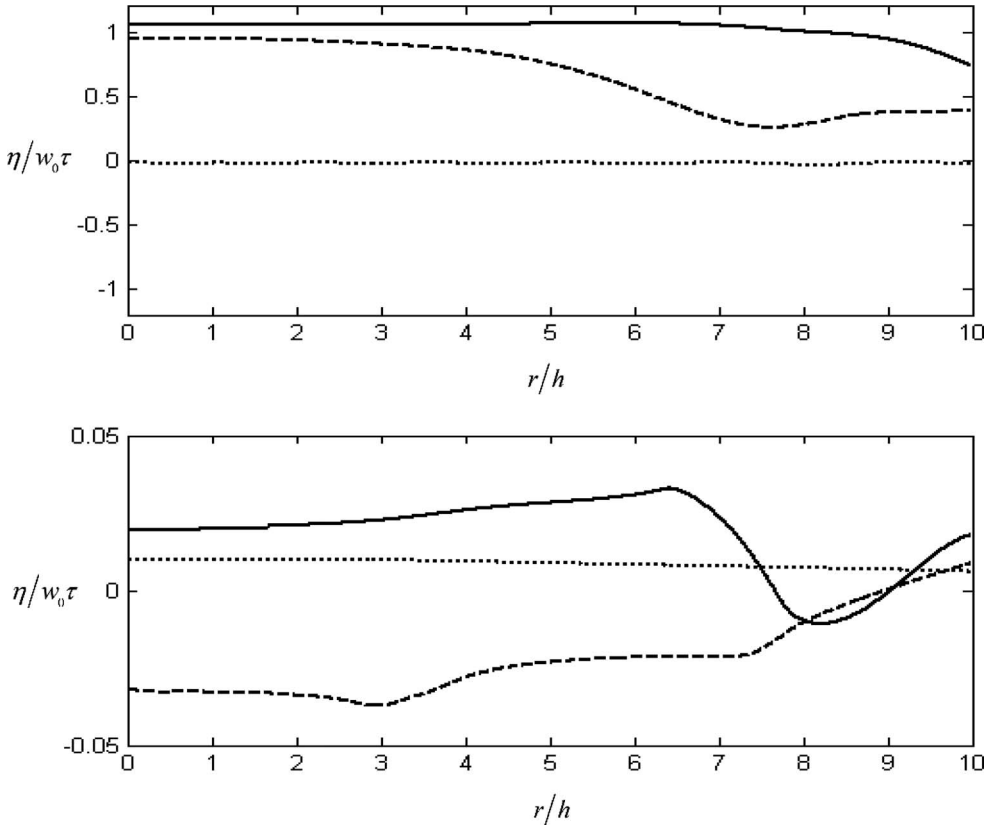

FIG. 2. The free-surface elevation $\eta(r, t)$ originated by a circular disturbance, in the inner region $r \leq R$, where depth $h = 4$ km, radius $R = 40$ km, duration $\tau = 10$ s, and speed $w_0 = 0.1$ m/s. Upper: Total elevation. Lower: 10 modes of Acoustic Gravity waves combined with 10 modes of evanescent waves. $t = \tau$ (solid), $t = 10\tau$ (dashed), $t = 100\tau$ (dotted).

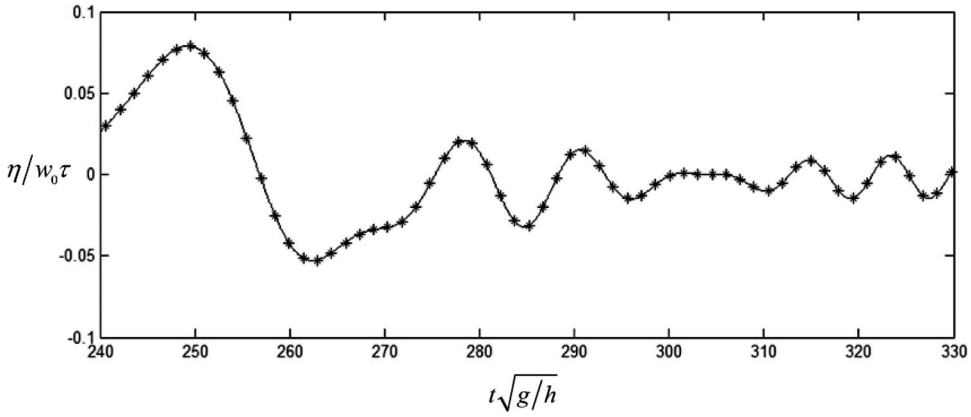

FIG. 3. The free-surface elevation $\eta(t)$ of the Tsunami, originated by a circular disturbance, as observed at radial distance $r = 1000$ km from epicenter. $\eta(t)$ was calculated by the first lines of the full solution (11b) (solid line) and of the Green function approach (21a) (asteriks) total overlapping, for depth $h = 4$ km, radius $R = 40$ km, $\tau = 10$ s, and speed $w_0 = 0.1$ m/s. The original disturbance was divided into 5041 equal elements, each with an area of 1 km^2. The time interval is (4600 s–6600 s).

B. Validation of the Green function and of the Stationary-Phase approaches

The validity of the Green Function approach and the usefulness of the Stationary-Phase method are demonstrated in Figures 3 and 4. Figure 3 gives the results for the Tsunami, whereas Figure 4 focuses on the Acoustic-Gravity waves.

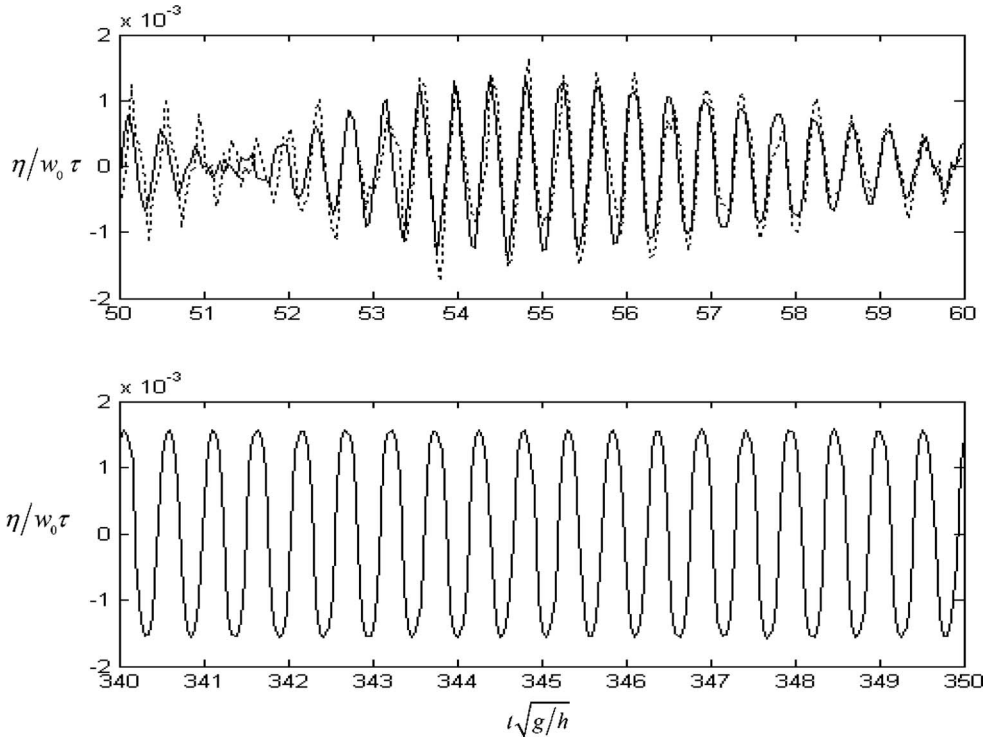

FIG. 4. The free surface elevation caused by 10 modes of Acoustic-Gravity waves that originated by a circular disturbance. Observation was made at radial distance $r = 1000$ km from epicenter. The Acoustic-Gravity waves at 1000 km, as calculated by the second line of the full solution (11b) using the Stationary-Phase approach (solid line) and by the Green function approach (21a) (dashed line), for depth $h = 4$ km, radius $R = 40$ km, duration $\tau = 10$ s, and speed $w_0 = 0.1$ m/s. Upper: for the time interval (1000 s–1200 s) one sees some differences. Lower: for the time interval (6800 s–7000 s) total overlapping. For the Green function calculations the original disturbance was divided into 5041 equal elements, each with an area of 1 km^2.

At this stage it is worthwhile to point out that the validity of the Green Function can be proven analytically, but the graphic results strengthen our confidence also in its numerical implementation. In Sec. VI we apply the Green Function approach to rectangular disturbances.

Experiments with different element sizes in the Green Function method confirm that element area of 1 km^2 provides reasonable description of the radiation field. Figure 3 shows a full agreement between both methods in the case of the Tsunami. For the Acoustic-Gravity waves, a small incompatibility appears in the short time interval, very close to the initial arrival time of the Acoustic-Gravity waves, but fades out with time, until total overlap is reached. Note that the overall agreement, as demonstrated in Figures 3 and 4, is rather satisfactory and strengthen our trust in the method and approximations proposed in Sec. IV.

VI. RESULTS FOR RECTANGULAR DISTURBANCE

Note that the following examples for rectangular disturbances are limited to constant disturbance velocity w_0, for simplicity. For a rectangular disturbance Eq. (6) is replaced by

$$\zeta_t = w_0 \cdot H\left(b^2 - x^2\right) \cdot H\left(a^2 - y^2\right) \cdot H\left[t\left(\tau - t\right)\right]. \tag{22}$$

In Figures 6–11 the time, surface elevation, and bottom pressure are presented in dimensional variables.

A. Comparison with previous work

In Figure 5 we compare the results for a slender rectangular disturbance with those for an infinitely long stripe given in Stiassnie.[9] The good compatibility between the 2 models demonstrates the strength of the Green Function method for handling general-shape disturbances. Some extent of inconsistency between the models is caused by the fact that the disturbances are rather similar but not identical.

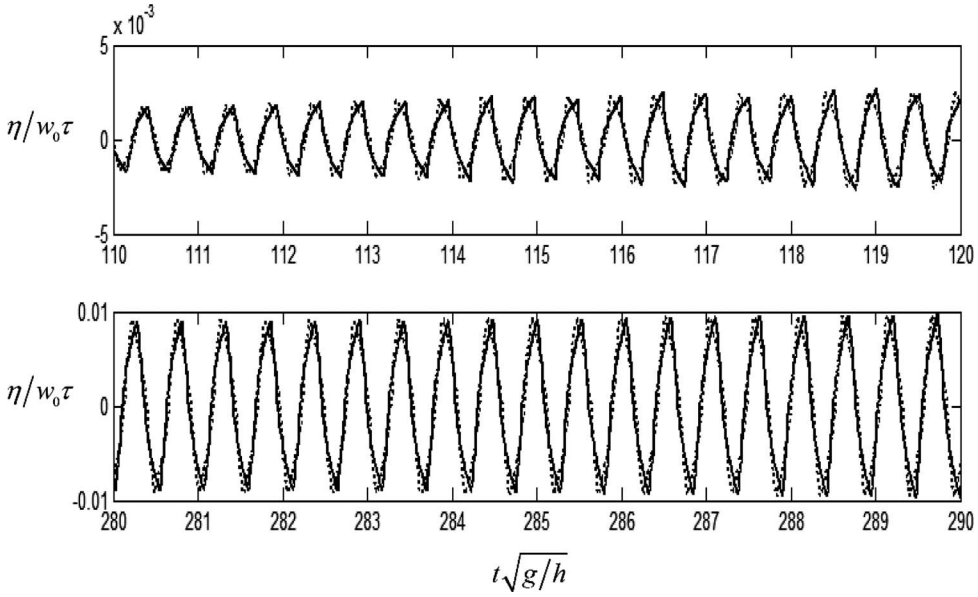

FIG. 5. The free surface elevation caused by 10 modes of Acoustic-Gravity waves, originated by a rectangular disturbance of 80 km × 4000 km (solid line) and an infinitely long stripe of 80 km width (dashed line). For both cases $h = 4$ km, $\tau = 10$ s, and speed $w_0 = 0.1$ m/s. Observations were taken at $x = 1000$ km and $y = 0$ for two time-intervals: upper (2200 s–2400 s) and lower (5600 s–5800 s). For the Green Function calculations the original disturbance was divided into 320 000 equal elements, each with an area of 1 km^2. Time steps was chosen to be 0.1 s.

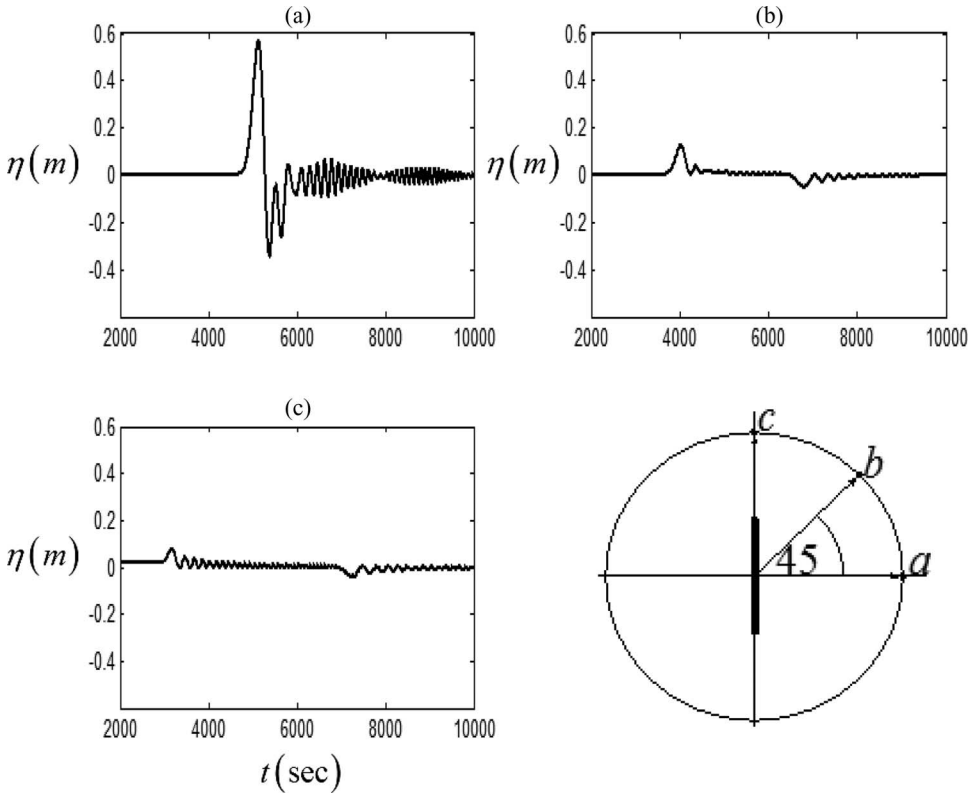

FIG. 6. The free-surface elevation of the Tsunami, originated by a rectangular disturbance of size 40 km × 800 km, depth: $h = 4$ km, duration $\tau = 10$ s, and speed $w_0 = 0.1$ m/s. Observations were taken at $x = r \cdot \cos(\theta)$, $y = r \cdot \sin(\theta)$, where $r = 1000$ km and $\theta = 0$ (a), $\theta = \pi/4$ (b), $\theta = \pi/2$ (c). The figure in the bottom right corner illustrates the locations of each observation point with respect to the rectangular disturbance, centered at the origin. For the Green Function calculations the original disturbance was divided into 32 000 equal elements, each with an area of 1 km^2.

B. New results for one rising slab

The free-surface elevations at three different locations and different time intervals, caused by a rectangular disturbance with $a = 400$ km and $b = 20$ km, are shown in Figure 6 for the Tsunami. Figures 7 and 8 show the bottom-pressure caused by the Acoustic-Gravity waves of the same rectangular disturbance.

From Figure 6, it is evident that the Tsunami surface elevation amplitude is decreasing when the angle of observation changes from 0° to 90°. On the other hand, the initial arrival time of the Tsunami to the observation point at radial distance r is $r/\sqrt{gh}$. Thus, for a depth of 4 km the Tsunami is expected to arrive to an observation point a after 4800 s, as shown in Figure 6(a). The arrival time decreases when the angle of observation changes from 0° to 90°, since the distance to the observation point is shorter for the upper half of the rectangle. It is smallest at observation point c, which is rather close to the minor face of the rectangular disturbance.

Figure 7 shows the bottom pressure oscillation due to the Acoustic-Gravity waves, originated by a rectangular disturbance, at 3 different observation points. The arrival times of the Acoustic-Gravity waves from the nearest/farthest element are marked by asterisk, and are (670 s, 720 s), (520 s, 880 s), and (400 s, 940 s) for points a, b, c, respectively. Note that the fact that the results in Figure 7 are drawn only for times larger than 720 s, 880 s, and 940 s for points a, b, c respectively, is a shortcoming of the approximation that we are using.

Figure 8 shows the time evolution of the same Acoustic-Gravity waves as in Figure 7 for the same observation points. Note that the amplitudes have stabilized at this stage and that they decrease with the increase of θ, just as with the Tsunami in Figure 6.

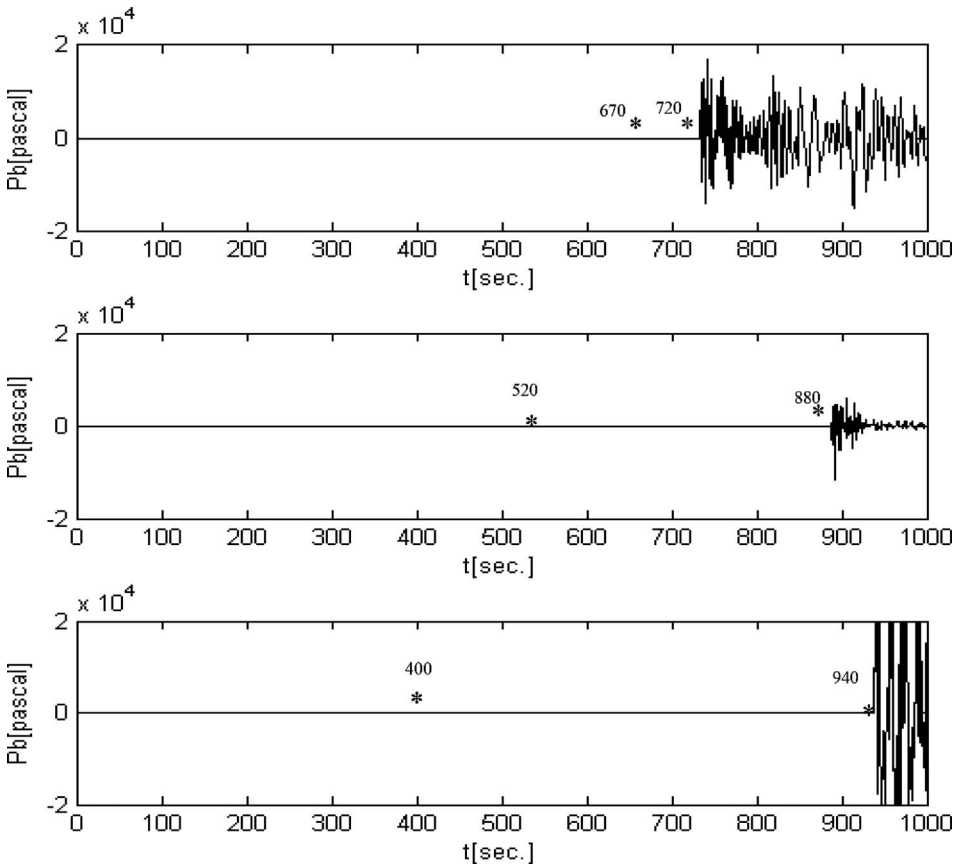

FIG. 7. The bottom pressure caused by 10 modes of Acoustic-Gravity waves, originating from a rectangular disturbance of size 40 km × 800 km, depth $h = 4$ km, duration $\tau = 10$ s, and speed $w_0 = 0.1$ m/s. Observations were taken at $x = r \cdot \cos(\theta)$, $y = r \cdot \sin(\theta)$, where $r = 1000$ km and $\theta = 0$ (upper), $\theta = \pi/4$ (middle), $\theta = \pi/2$ (bottom), as illustrated in the right bottom corner of Fig. 6. In each figure, the first asteriks indicate the theoretical arrival time of the wave, and the second asteriks indicate the instant prior to which the Stationary Phase approximation is meaningless.

C. New results for two adjacent slabs, one rising and the other descending

Figures 9–11 feature equivalent results as in Figures 6–8; only this time the rectangular disturbance is split lengthwise into 2 identical rectangles, each of $a = 400$ km $b = 10$ km, where the right one is moving upward and the left one is moving downward.

The observation points in Figures 9–11 were chosen to be in symmetry, so that one can see the upside down symmetry in the signals that were observed in point a (at an angle of 0°) and at point b (at angle of 180°), as well as between signals at point c (at an angle of 45°) and point d (at an angle of 135°). Figures 10 and 11 display the Acoustic-Gravity waves for the above 2 plates configuration, for short and long time intervals.

It is interesting to note that at the observation points with $r = 1000$ km the Tsunami amplitudes for one rising slab are larger than those for the two slabs (one rising and one descending); in contrast to the Acoustic-Gravity waves, for which this trend is reversed.

For an observation point at distance of the order of 1000 km the Acoustic-Gravity waves precede the Tsunami by the order of 4000 s. which can provide a Tsunami warning of more than 1 h.

A typical value for the free-surface amplitude of the Acoustic-Gravity waves is $A_s = 5 \times 10^{-3}$ m for $w_0\tau = 1$ m. The corresponding order of magnitude of the bottom pressure amplitude is $A_p = 5000$ Pa ≈ 0.05 atm which is considered as measurable.

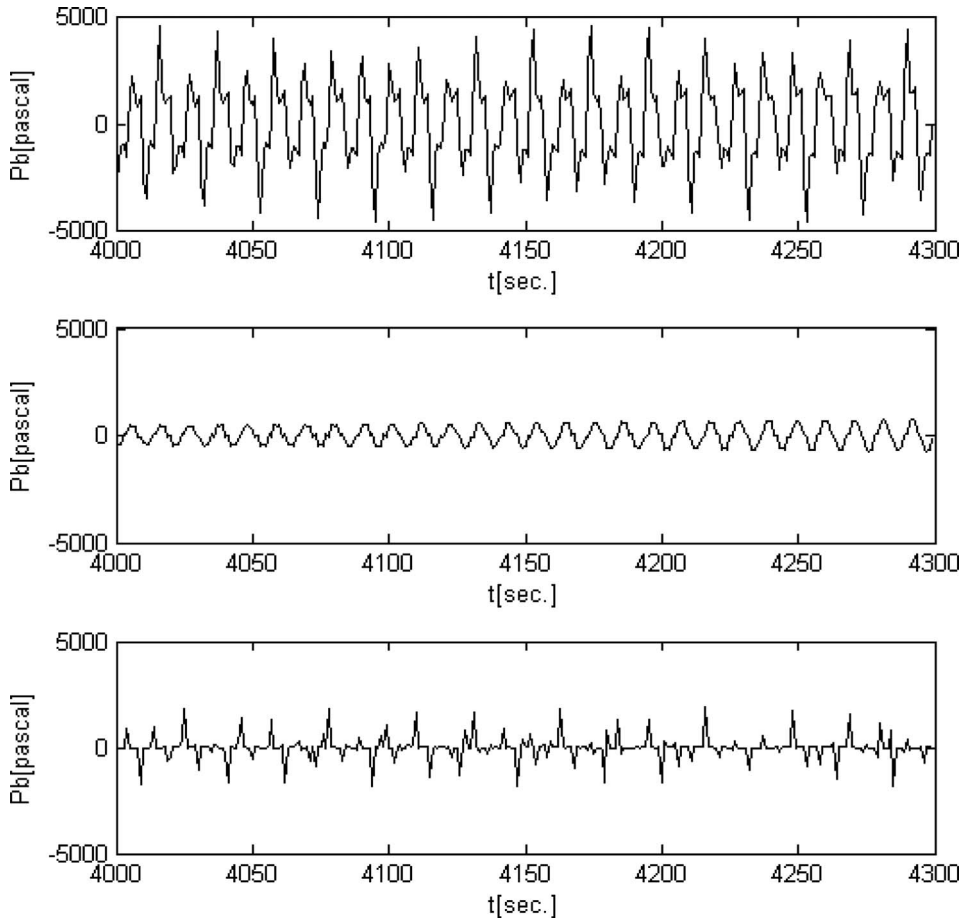

FIG. 8. The bottom pressure caused by 10 modes of Acoustic-Gravity waves, originating from a rectangular disturbance of size 40 km × 800 km, depth $h = 4$ km, duration $\tau = 10$ s, and speed $w_0 = 0.1$ m/s. Observations were taken at $x = r \cdot \cos(\theta)$, $y = r \cdot \sin(\theta)$, where $r = 1000$ km and $\theta = 0$ (upper), $\theta = \pi/4$ (middle), $\theta = \pi/2$ (bottom), as illustrated in the right bottom corner of Fig. 6.

VII. DISCUSSION AND OUTLINE OF THE INVERSE PROBLEM TREATMENT

In this paper we have demonstrated how one can calculate the Tsunami, as well as the Acoustic-Gravity waves, that radiate from a rather general bottom disturbance generated by an underwater earthquake in an ocean of otherwise constant depth.

We have also shown that the Acoustic-Gravity waves, which propagate about seven times faster than the Tsunami, generate a significant pressure signal at the bottom, which could be used for early Tsunami detection. Such a procedure requires the development of an approach to solve the inverse problem, namely, the specifying of the earthquake parameters from measured bottom pressure records.

In the sequel we outline one possible, rather simplified, procedure.

Assuming a circular disturbance of radius R, duration τ, and vertical velocity w_0, according to Eqs. (11b) and (5), after application of the Stationary-Phase method (Carrier *et al.*,[11] Sec. 6-4), the leading Acoustic-Gravity mode of the bottom pressure gives

$$P_b = \frac{8\rho c R w_0}{\pi r} \cdot \sin(\hat{\omega}_1 \tau/2) \cdot J_1(R\hat{q}_1) \cdot \cos(\hat{q}_1 r - \hat{\omega}_1 t). \tag{23}$$

Denoting the unknown epicenter coordinates by (x_0, y_0), the unknown instant of the earthquake occurrence time by t_0, and assuming a circular disturbance, yields a set of six unknown earthquake parameters: x_0, y_0, t_0, R, w_0, and τ. These can be retrieved from measurements in two stations: A

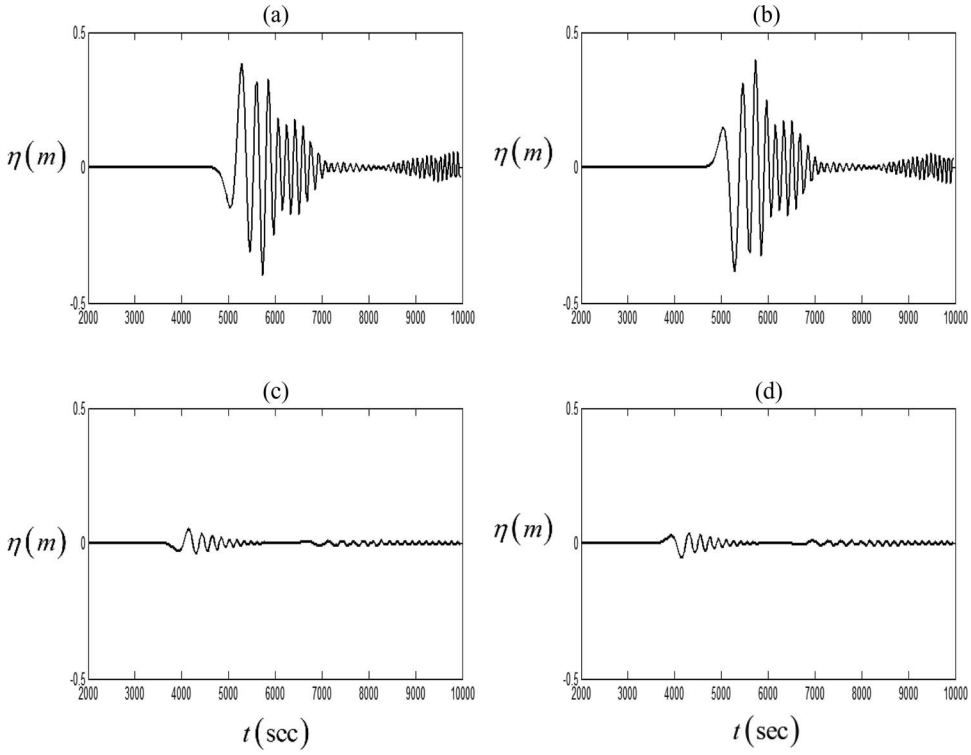

FIG. 9. The surface elevation caused by the Tsunami originating from a rectangular disturbance composed of 2 rectangles each of size 20 km × 800 km, where the right one moves upward and the left one moves downward. Depth $h = 4$ km, duration $\tau = 10$ s, and speed $w_0 = \pm 0.1$ m/s. The results are shown at $x = r \cdot \cos(\theta)$, $y = r \cdot \sin(\theta)$, where $r = 1000$ km and $\theta = 0$ (a), $\theta = \pi$ (b), $\theta = \pi/4$ (c), $\theta = 3\pi/4$ (d).

and B located at coordinates (x_A, y_A) and (x_B, y_B). Two measurements are performed in each station at 2 instances, denoted as t_{A1} and t_{A2} for station A, and t_{B1} and t_{B2} for station B. The measured data include the bottom pressure amplitudes and frequencies as summarized in Table I.

We suggest the following procedure, split into 2 steps, for extracting the earthquake parameters.

Step 1: determination of epicenter location and time of occurrence

The time instances (t_{A1}, t_{A2}) and the appropriate frequencies $(\omega_{A1}, \omega_{A2})$ are substituted into (20a) to provide a system of two linear equations for the time of earthquake occurrence that was intercepted by station A, t_{A0}, and for the radial distance of station A from the epicenter, r_A:

$$\hat{\omega}_{A1} = \frac{\pi c}{h\sqrt{1 - [r_A/c\,(t_{A1} - t_{A0})]^2}}, \tag{24a}$$

$$\hat{\omega}_{A2} = \frac{\pi c}{h\sqrt{1 - [r_A/c\,(t_{A2} - t_{A0})]^2}}. \tag{24b}$$

Performing the above procedure also to station B yields the following set of values: t_{A0}, t_{B0}, r_A, and r_B. To find the location of the epicenter one has to find the appropriate intersection point of the

TABLE I. Measured data notations.

Location	Time	Amplitude	Frequency
A	$t = t_{A1}$	a_{A1}	ω_{A1}
	$t = t_{A2}$	a_{A2}	ω_{A2}
B	$t = t_{B1}$	a_{B1}	ω_{B1}
	$t = t_{B2}$	a_{B2}	ω_{B2}

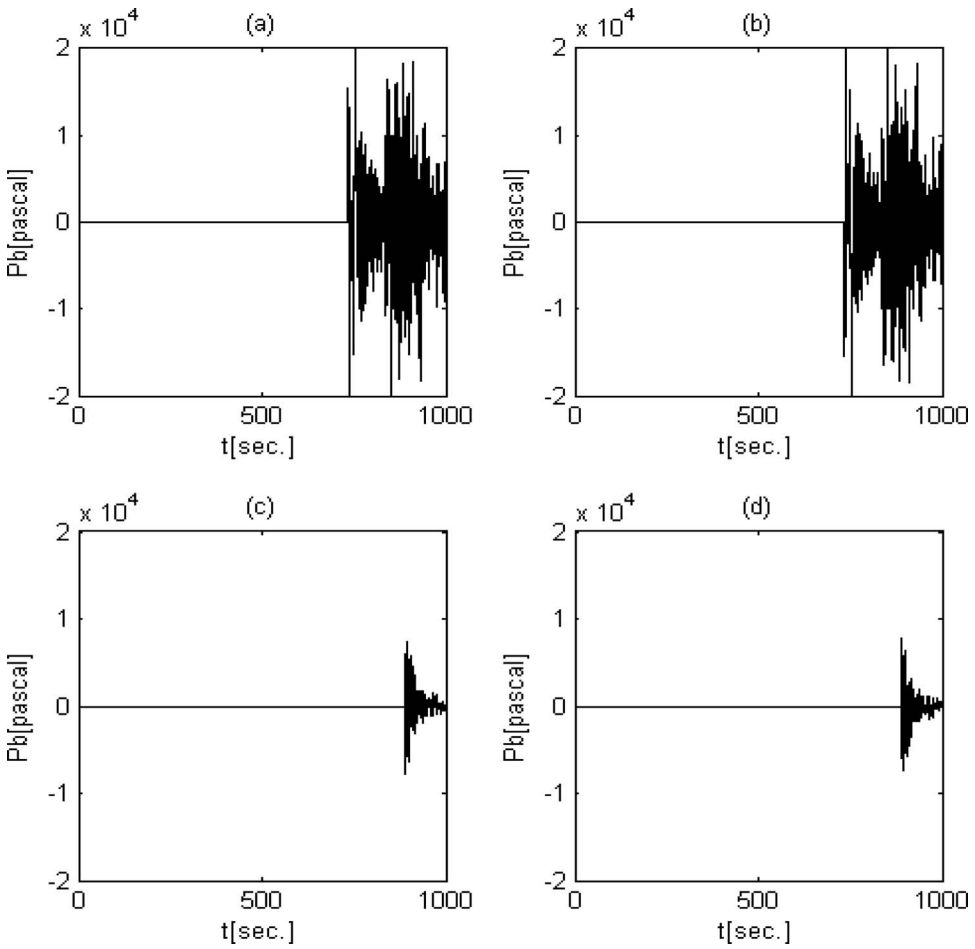

FIG. 10. The bottom pressure caused by 10 modes of Acoustic-Gravity waves originating from a rectangular disturbance composed of 2 rectangles each of size 20 km × 800 km, where the right one moves upward and the left one moves downward. Depth $h = 4$ km, duration $\tau = 10$ s, and speed $w_0 = \pm 0.1$ m/s. The results are shown at $x = r \cdot \cos(\theta)$, $y = r \cdot \sin(\theta)$, where $r = 1000$ km and $\theta = 0$ (a), $\theta = \pi$ (b), $\theta = \pi/4$ (c), $\theta = 3\pi/4$ (d).

following two circles:

$$(x_A - x_0)^2 + (y_A - y_0)^2 = r_A^2, \tag{25a}$$

$$(x_B - x_0)^2 + (y_B - y_0)^2 = r_B^2. \tag{25b}$$

Although the solution of (25a) and (25b) yields 2 sets of values for (x_0, y_0), it is most likely that practically one of the solutions can be discarded, based on geographical considerations.

Step 2: determination of disturbance duration, radius, and vertical velocity

In order to avoid an implicit expression for the disturbance duration τ, we let $R \to 0$ in (23) to obtain

$$P_b = \frac{2\rho c R^2 w_0}{rh\sqrt{(ct/r)^2 - 1}} \cdot \sin(\hat{\omega}_1 \tau/2) \cdot \cos(\hat{q}_1 r - \hat{\omega}_1 t). \tag{26}$$

Provided the data measurements from both stations A and B and the calculations from step 1 for t_{A0}, t_{B0}, r_A, and r_B, one can write the following system of 2 equations for each station, for the

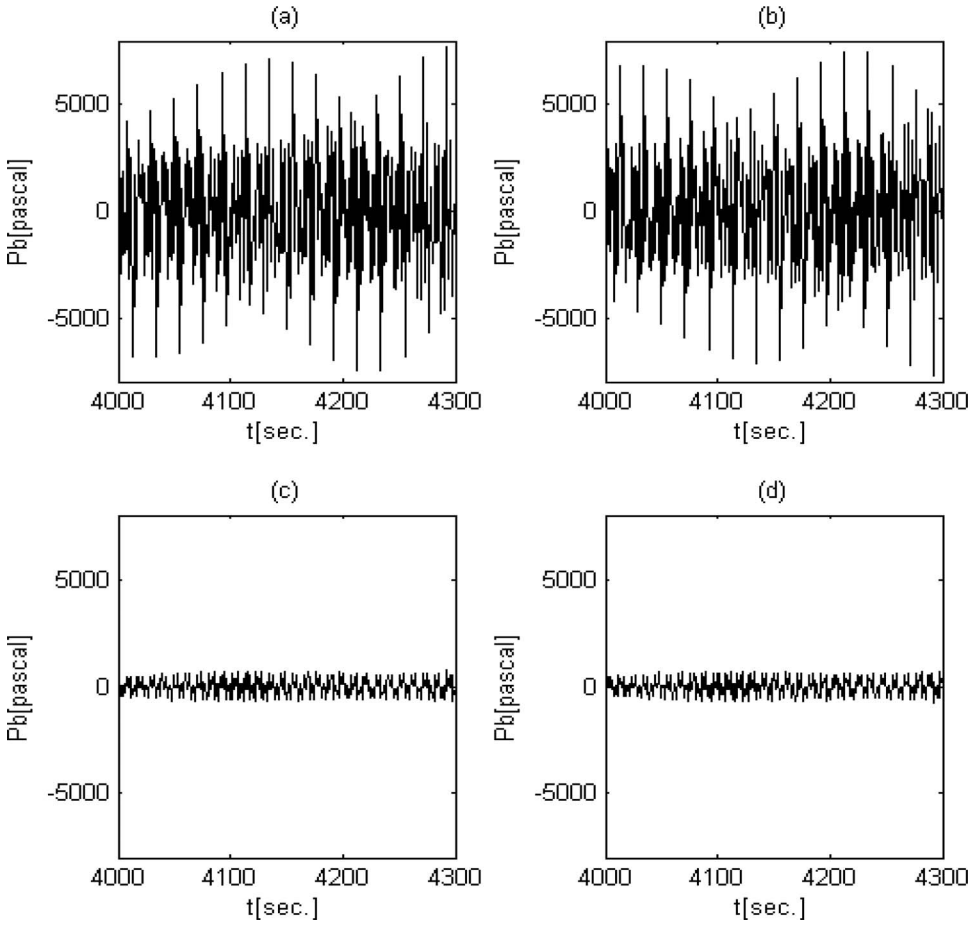

FIG. 11. The bottom pressure caused by 10 modes of Acoustic-Gravity waves originating from a rectangular disturbance composed of 2 rectangles each of size 20 km × 800 km, where one is moving upward and the other moves downward. Depth $h = 4$ km, duration $\tau = 10$ s, and speed $w_0 = \pm 0.1$ m/s. The results shown at $x = r \cdot \cos(\theta)$, $y = r \cdot \sin(\theta)$, where $r = 1000$ km and $\theta = 0$ (a), $\theta = \pi$ (b), $\theta = \pi/4$ (c), $\theta = 3\pi/4$ (d).

earthquake duration τ:

$$\tilde{a}_{A1} = \frac{2\rho c w_0 R^2}{h r_A \sqrt{[c\,(t_{A1} - t_{0A})/r_A]^2 - 1}} \cdot \sin(\omega_{A1}\tau_A/2)\,, \tag{27a}$$

$$\tilde{a}_{A2} = \frac{2\rho c w_0 R^2}{h r_A \sqrt{[c\,(t_{A2} - t_{0A})/r_A]^2 - 1}} \cdot \sin(\omega_{A2}\tau_A/2)\,. \tag{27b}$$

τ_A is calculated numerically from the quotient of (27a) and (27b). τ_A is then substituted in (23) to obtain the disturbance radius R_A from the quotient of the set

$$a_{A1} = \frac{8\rho c R_A w_0}{\pi r_A} \cdot \sin(\omega_{A1}\tau_A/2) \cdot J_1(R_A q_{A1})\,, \tag{28a}$$

$$a_{A2} = \frac{8\rho c R_A w_0}{\pi r_A} \cdot \sin(\omega_{A2}\tau_A/2) \cdot J_1(R_A q_{A2})\,. \tag{28b}$$

Once τ_A and R_A are determined, the vertical velocity w_0 is calculated from (28a) and (28b) to obtain 2 values: w_{0A1}, w_{0A2}. A similar procedure applied to the data of point B will give τ_B, R_B and w_{0B1}, w_{0B2}. Generally speaking, one would expect all values of t_0, τ, R, w_0 to be equal for both points A and B. For practical applications one could take $t_0 = (t_{0A} + t_{0B})/2$, $\tau = (\tau_A + \tau_B)/2$, $R = (R_A + R_B)/2$, and $w_0 = (w_{0A1} + w_{0A2} + w_{0B1} + w_{0B2})/4$.

TABLE II. Comparison between model input parameters and inverse calculation results.

		Input parameters	Inverse process parameters
Distance between epicenter and station A	r_A	1000 km	1084 km
Distance between epicenter and station B	r_B	1500 km	1548 km
Epicenter location	x_0, y_0	0, 0	0, 0
Earthquake occurrence time	t_0	0 s	−81.24 s
Disturbance radius	R	40000 m	40547 m
Disturbance duration	τ	10 s	10.82 s
Disturbance vertical velocity	w_0	0.1 m/s	0.107 m/s

A numerical example based on the above procedure demonstrates a reasonable recovery of the earthquake parameters. We have chosen a circular disturbance as the input to the model to produce an artificial data. The inverse process results are summarized in Table II.

To recover more general disturbances we intend to extend the proposed approach from circular to elliptical earthquakes. As a first step in this direction the counterpart of Eqs. (11a) and (11b) for an elliptical disturbance is given in Appendix A.

ACKNOWLEDGMENTS

This research was supported by the Israel Science Foundation (Grant No. 63/09). The research is part of a Ph.D. thesis submitted by G.H. to the Graduate School of the Technion – Israel Institute of Technology.

APPENDIX A: SOLUTION FOR AN ELLIPTICAL DISTURBANCE

The inverse problem solution that was outlined in Sec. VII is limited to a circular disturbance only. In order to provide a more general solution for future work, we suggest a new model, where the circular shaped disturbance of radius R is replaced by an elliptical shaped disturbance with semi-major axis R_1 and semi-minor axis R_2, so that $R_1 = a \cdot \cosh(R)$, $R_2 = a \cdot \sinh(R)$, where a is half of the inter-focal distance. By solving Eq. (1) and boundary conditions (2) and (3) for the elliptical model, the expressions for the potential field in the inner region (above the elliptical disturbance) and the outer region (outside the elliptical disturbance) are derived, where the parameter R is the radial coordinate of the elliptical boundary. Note that the potential of the elliptical disturbance is given in terms of the elliptic cylindrical coordinates (r, θ, z) and Mathieu functions ce_{2m}, Ce_{2m}, Fey_{2m}, and Fek_{2m}, see McLachlan:[13]

$$\Phi_{in}(z, r, \theta, t) =$$

$$\frac{2a^2 w_0}{\pi^2} \sum_{m=0}^{\infty} \int_0^{\infty} \frac{\left[Fey'_{2m}(R, q_0) \cos\left(\omega t - \frac{\omega\tau}{2}\right) - Ce'_{2m}(R, q_0) \sin\left(\omega t - \frac{\omega\tau}{2}\right) \right] \cdot \int_0^{2\pi} ce_{2m}(\theta, q_0)\, d\theta}{Ce'_{2m}(R, q_0)\, Fey_{2m}(R, q_0) - Ce_{2m}(R, q_0)\, Fey'_{2m}(R, q_0)} \cdot$$

$$\frac{\mu_0 \cosh[\mu_0 (z + h)] \cdot \sin\left(\frac{\omega\tau}{2}\right)}{\omega q_0 [2\mu_0 h + \sinh(2\mu_0 h)]} \cdot Ce_{2m}(r, q_0)\, ce_{2m}(\theta, q_0)\, d\omega$$

$$+ \frac{2a^2 w_0}{\pi^2} \sum_{n=1}^{N} \sum_{m=0}^{\infty} \int_{\omega_{sn}}^{\infty} \frac{\left[Fey'_{2m}(R, q_n) \cos\left(\omega t - \frac{\omega\tau}{2}\right) - Ce'_{2m}(R, q_n) \sin\left(\omega t - \frac{\omega\tau}{2}\right) \right] \cdot \int_0^{2\pi} ce_{2m}(\theta, q_n)\, d\theta}{Ce'_{2m}(R, q_n)\, Fey_{2m}(R, q_n) - Ce_{2m}(R, q_n)\, Fey'_{2m}(R, q_n)} \cdot$$

$$\frac{\mu_n \cos[\mu_n (z + h)] \cdot \sin\left(\frac{\omega\tau}{2}\right)}{\omega q_n [2\mu_n h + \sin(2\mu_n h)]} \cdot Ce_{2m}(r, q_n)\, ce_{2m}(\theta, q_n)\, d\omega$$

$$-\frac{2a^2w_0}{\pi^2}\sum_{n=N+1}^{\infty}\sum_{m=0}^{\infty}\int_0^{\omega_{sn}}\frac{Fek'_{2m}(R,q_n)\cdot\cos\left(\omega t-\frac{\omega\tau}{2}\right)\cdot\int_0^{2\pi}ce_{2m}(\theta,q_n)\,d\theta}{Ce'_{2m}(R,q_n)\,Fek_{2m}(R,q_n)-Ce_{2m}(R,q_n)\,Fek'_{2m}(R,q_n)}\cdot$$
$$\frac{\mu_n\cos[\mu_n(z+h)]\cdot\sin\left(\frac{\omega\tau}{2}\right)}{\omega q_n[2\mu_n h+\sin(2\mu_n h)]}Ce_m(r,q_n)\,ce_m(\theta,q_n)\,d\omega$$
$$+\frac{2w_0}{\pi}\int_0^{\infty}\sin\left(\frac{\omega\tau}{2}\right)\cos\left(\omega t-\frac{\omega\tau}{2}\right)\cdot\frac{\frac{c}{g}\sin\left(\frac{\omega}{c}z\right)+\frac{1}{\omega}\cos\left(\frac{\omega}{c}z\right)}{\frac{\omega}{c}\sin(\frac{\omega}{c}h)+\frac{\omega^2}{g}\cos(\frac{\omega}{c}h)+}d\omega, \tag{A1}$$

$$\Phi_{out}(z,r,\theta,t)=$$

$$\frac{2a^2w_0}{\pi^2}\sum_{m=0}^{\infty}\int_0^{\infty}\frac{\mu_0\cosh[\mu_0(z+h)]\cdot\sin\left(\frac{\omega\tau}{2}\right)}{\omega q_0[2\mu_0 h+\sinh(2\mu_0 h)]}\cdot\frac{Ce'_{2m}(R,q_0)\cdot\int_0^{2\pi}ce_{2m}(\theta,q_0)\,d\theta}{Ce'_{2m}(R,q_0)\,Fey_{2m}(R,q_0)-Ce_{2m}(R,q_0)\,Fey'_{2m}(R,q_0)}\cdot$$
$$\cdot\left[Fey_{2m}(r,q_0)\cos\left(\omega t-\frac{\omega\tau}{2}\right)-Ce_{2m}(r,q_0)\sin\left(\omega t-\frac{\omega\tau}{2}\right)\right]ce_{2m}(\theta,q_0)\,d\omega$$

$$+\frac{2a^2w_0}{\pi^2}\sum_{n=1}^{N}\sum_{m=0}^{\infty}\int_{\omega_{sn}}^{\infty}\frac{\mu_n\cos[\mu_n(z+h)]\cdot\sin\left(\frac{\omega\tau}{2}\right)}{\omega q_n[2\mu_n h+\sin(2\mu_n h)]}\cdot\frac{Ce'_{2m}(R,q_n)\cdot\int_0^{2\pi}ce_{2m}(\theta,q_n)\,d\theta}{Ce'_{2m}(R,q_n)\,Fey_{2m}(R,q_n)-Ce_{2m}(R,q_n)\,Fey'_{2m}(R,q_n)}\cdot$$
$$\left[Fey_{2m}(r,q_n)\cos\left(\omega t-\frac{\omega\tau}{2}\right)-Ce_{2m}(r,q_n)\sin\left(\omega t-\frac{\omega\tau}{2}\right)\right]ce_{2m}(\theta,q_n)\,d\omega$$

$$-\frac{2a^2w_0}{\pi^2}\sum_{n=N+1}^{\infty}\sum_{m=0}^{\infty}\int_0^{\omega_{sn}}\frac{\mu_n\cos[\mu_n(z+h)]\cdot\sin\left(\frac{\omega\tau}{2}\right)}{\omega q_n[2\mu_n h+\sin(2\mu_n h)]}\cdot\frac{Ce'_{2m}(R,q_n)\cdot\int_0^{2\pi}ce_{2m}(\theta,q_n)\,d\theta}{Ce'_{2m}(R,q_n)\,Fek_{2m}(R,q_n)-Ce_{2m}(R,q_n)\,Fek'_{2m}(R,q_n)}\cdot$$
$$Fek_{2m}(r,q_n)\cos\left(\omega t-\frac{\omega\tau}{2}\right)ce_{2m}(\theta,q_n)\,d\omega. \tag{A2}$$

Note that Ce', Fey', and Fek' are the derivatives with respect to r of these functions. Also note that the q_ns in (A1) and (A2) are $(a^2/4)$ times the squares of the q_ns in (13a)–(13c).

APPENDIX B: OUTLINE OF THE MATHEMATICAL PROCEDURE FOR THE SOLUTION OF THE CIRCULAR DISTURBANCE PROBLEM

In order to obtain the velocity potential field described in (11a) and (11b), a second order partial equation must be solved. Starting with a cylindrical wave equation model, the method of separation of variables will be used for separating its radial and depth dimensions. The velocity potential is then obtained from its independent components for the inner and outer regions separately. The solution is first obtained in the frequency domain using Inverse Fourier Transform. Then, by using circular symmetry the full solution is obtained for inner and outer regions. The significance of this stage is the ability to obtain the spatial and temporal velocity potential field later being used for deriving the expressions for water surface elevation and bottom pressure.

The Fourier transform of the velocity potential in cylindrical coordinates is defined by

$$\tilde{\Phi}(r,z,\omega)=\frac{1}{\sqrt{2\pi}}\int_{-\infty}^{\infty}\Phi(r,z,t)e^{-i\omega t}dt. \tag{B1}$$

Taking the Fourier transform of the governing Eq. (1), as well as of the linear boundary conditions (2) and (3), reduces to the Helmholtz equation with the following boundary conditions:

$$\nabla^2\tilde{\Phi} = -\frac{\omega^2}{c^2}\tilde{\Phi}, \tag{B2}$$

$$\tilde{\Phi}_z = \frac{\omega^2}{g}\tilde{\Phi}\Big|_{z=0}, \tag{B3}$$

$$\tilde{\Phi}_z = \tilde{w}_0(r,\omega)\big|_{z=-h}, \tag{B4}$$

where $\tilde{\Phi}$, $\tilde{w}_0$ denotes the Fourier transform of Φ, w_0, respectively, and

$$\tilde{w}_0(r,\omega) = \frac{1}{\sqrt{2\pi}}\int_{-\infty}^{\infty} w_0(r,t)e^{-i\omega t}dt = \frac{i\zeta_0}{\tau\sqrt{2\pi}}H\left(R^2-r^2\right)\frac{e^{-i\omega\tau}-1}{\omega}. \tag{B5}$$

Assuming independency of spatial variables r and z the transformed potential $\tilde{\Phi}$ can be written as a product of 2 functions $\bar{R}$ and $\bar{Z}$:

$$\tilde{\Phi}(r,z,\omega) = \bar{R}(r,\omega)\,\bar{Z}(z,\omega). \tag{B6}$$

Differentiation of (B6) and substituting into (B2) yields a set of 2 ordinary differential equations:

$$\bar{Z}_{zz} + \left(\frac{\omega^2}{c^2}+\alpha_3\right)\bar{Z} = 0, \tag{B7}$$

$$\bar{R}_{rr} + \frac{1}{r}\bar{R}_r - \alpha_3\bar{R} = 0. \tag{B8}$$

The lower index refers to the partial derivative with respect to index. α_3 is the separation constant between r and z.

The solution in the vertical direction z depends on the separation constant α_3. According to Moon and Spencer (1961) when choosing $\alpha_3 = q^2$, the general solution to (B7) becomes

$$\bar{Z} = C_1\sin[\mu z] + C_2\cos[\mu z], \tag{B9}$$

$$\mu = \sqrt{\frac{\omega^2}{c^2}+q^2}. \tag{B10}$$

Application of the boundary conditions (B3) and (B4) for (B9) results in the dispersion equation:

$$\mu\cdot\tan(\mu h) = -\frac{\omega^2}{g}. \tag{B11}$$

A comprehensive examination of the numerical (or graphical) solutions of (B11) reveals one imaginary root, designated as μ_0, and an infinite set of real roots designated as μ_n, which are divided into 2 types. The complete set of roots, known as wave modes, is summarized in Table III. The interpretation as progressive or evanescent wave modes evolves from the analysis of the solution in the radial direction.

TABLE III. Wave mode types according to dispersion equation roots.

Mode index	Mode's wave number	Modes type
$n=0$	$q_0 = i\sqrt{(\omega/c)^2+\mu_0^2}$	Imaginary μ and q, propagating gravity wave (Tsunami)
$n=1,\ldots,N$	$q_n = i\sqrt{(\omega/c)^2-\mu_n^2}$	Real μ and imaginary q, propagating acoustic-gravity waves
$n=N+1,\ldots,\infty$	$q_n = \sqrt{\mu_n^2-(\omega/c)^2}$	Real μ and q, non-propagating (evanescent) waves

For the outer (or inner region) these Eigenfunctions are as follows:
For the outer region:

$$A_0 \frac{\cosh\left[\mu_0 (z+h)\right]}{\cosh\left(\mu_0 h\right)}; \quad A_n \frac{\cos\left[\mu_n (z+h)\right]}{\cos\left(\mu_n h\right)}\Bigg|_{n=1,\ldots,\infty}. \tag{B12}$$

For the inner region:

$$B_0 \frac{\cosh\left[\mu_0 (z+h)\right]}{\cosh\left(\mu_0 h\right)}; \quad B_n \frac{\cos\left[\mu_n (z+h)\right]}{\cos\left(\mu_n h\right)}\Bigg|_{n=1,\ldots,\infty}. \tag{B13}$$

For the inner region one also has to add the following particular solution:

$$g(z) = \frac{icw_0}{\sqrt{2\pi}} \cdot \frac{e^{-i\omega\tau} - 1}{\omega^2} \cdot \frac{\omega c \cdot \sin\left(\frac{\omega}{c} z\right) + g \cdot \cos\left(\frac{\omega}{c} z\right)}{g \cdot \sin\left(\frac{\omega}{c} h\right) + \omega c \cdot \cos\left(\frac{\omega}{c} h\right)}. \tag{B14}$$

The solution in the radial direction r is established in the inner and outer regions, according to the particular boundary conditions. In addition, the parameter q determines whether a specific mode is progressive or evanescent. The general solution for the radial ordinary differential equation (B8), as suggested by Moon and Spencer,[14] is a linear combination of Bessel functions J_0 and Y_0:

$$\bar{R} = F_1 J_0 (iqr) + F_2 Y_0 (iqr). \tag{B15}$$

F_1, F_2 are general coefficients. For the Tsunami and Acoustic-Gravity modes, when $n = 0, \ldots, N$, q_n is pure imaginary, thus the argument of the Bessel functions is real, resulting in oscillatory progressive modes. For the evanescent modes, when $n = N+1, \ldots, \infty$, q_n is real, the Bessel functions become Modified Bessel functions, resulting in non-progressing modes:

$$\begin{aligned} J_0 (iq_n r) &= I_0 (q_n r), \\ Y_0 (iq_n r) &= K_0 (q_n r). \end{aligned} \tag{B16}$$

The transformed potential $\tilde{\Phi}$ is constructed from its independent parts for the inner region and for the outer region separately.

In the inner region the assembled potential is

$$\begin{aligned} \tilde{\Phi}_{in} (r, z, \omega) &= A_0 J_0 (q_0 r) \cosh\left[\mu_0 (z+h)\right] + \sum_{n=1}^{N} A_n J_0 (q_n r) \cos\left[\mu_n (z+h)\right] \\ &+ \sum_{n=N+1}^{\infty} A_n I_0 (q_n r) \cos\left[\mu_n (z+h)\right] + g(z). \end{aligned} \tag{B17}$$

In the outer region the assembled potential is

$$\begin{aligned} &\tilde{\Phi}_{out} (r, z, \omega) = B_0 H_0^{\left[1.5+0.5\mathrm{sgn}(\omega)\right]} (q_0 r) \cosh\left[\mu_0 (z+h)\right] + \\ &\sum_{n=1}^{N} B_n H_0^{\left[1.5+0.5\mathrm{sgn}(\omega)\right]} (q_n r) \cos\left[\mu_n (z+h)\right] + \sum_{n=N+1}^{\infty} B_n K_0 (q_n r) \cos\left[\mu_n (z+h)\right], \end{aligned} \tag{B18}$$

where $H_0^{\left[1.5+0.5\mathrm{sgn}(\omega)\right]}$ represents the Hankel function as a function of propagation direction according to

$$\begin{aligned} H_0^{(1)} (q_n r) &= J_0 (q_n r) + i Y_0 (q_n r), \\ H_0^{(2)} (q_n r) &= J_0 (q_n r) - i Y_0 (q_n r). \end{aligned} \tag{B19}$$

The set of coefficients A_0, A_n and B_0, B_n are computed by applying the continuity conditions on the boundary that separates the outer region from the inner region, i.e., $r = R$:

$$\tilde{\Phi}_{in}\big|_{r=R} = \tilde{\Phi}_{out}\big|_{r=R}, \tag{B20}$$

$$\frac{d\tilde{\Phi}_{in}}{dr}\bigg|_{r=R} = \frac{d\tilde{\Phi}_{out}}{dr}\bigg|_{r=R}. \tag{B21}$$

In order to calculate the coefficients, $\tilde{\Phi}_{in}$, $\tilde{\Phi}_{out}$ need to be multiplied by the vertical Eigen functions (B12) and (B13) and integrated for the interval of orthogonality $[-h, 0]$. Thus, the expressions for the transformed potential in the inner and outer regions are obtained:

$$\begin{aligned}
\tilde{\Phi}_{in}(r,z,\omega) = &-\sqrt{2\pi}Rw_0 \cdot \frac{\mu_0 \cosh[\mu_0(z+h)]}{q_0[\sinh(2\mu_0 h)+2\mu_0 h]} \cdot \\
&\frac{\operatorname{sgn}(\omega)\cdot\left(e^{-i\omega\tau}-1\right)}{\omega} \cdot J_0(q_0 r) \cdot H_1^{[1.5+0.5\operatorname{sgn}(\omega)]}(q_0 R) \\
&-\sqrt{2\pi}Rw_0 \sum_{n=1}^{N} \frac{\mu_n \cos[\mu_n(z+h)]}{q_n[\sin(2\mu_n h)+2\mu_n h]} \cdot \\
&\frac{\operatorname{sgn}(\omega)\cdot\left(e^{-i\omega\tau}-1\right)}{\omega} \cdot J_0(q_n r) \cdot H_1^{[1.5+0.5\operatorname{sgn}(\omega)]}(q_n R) \\
&+\frac{4Rw_0 i}{\sqrt{2\pi}} \sum_{n=N+1}^{\infty} \frac{\mu_n \cos[\mu_n(z+h)]}{q_n[\sin(2\mu_n h)+2\mu_n h]} \cdot \\
&\frac{e^{-i\omega\tau}-1}{\omega} \cdot I_0(q_n r) K_1(q_n R) + g(z),
\end{aligned} \tag{B22}$$

where $g(z)$ is given in (B14):

$$\begin{aligned}
\tilde{\Phi}_{out}(r,z,\omega) = &-\sqrt{2\pi}Rw_0 \cdot \frac{\mu_0 \cosh[\mu_0(z+h)]}{q_0[\sinh(2\mu_0 h)+2\mu_0 h]} \cdot \\
&\frac{\operatorname{sgn}(\omega)\cdot\left(e^{-i\omega\tau}-1\right)}{\omega} \cdot J_1(q_0 R) H_0^{[1.5+0.5\operatorname{sgn}(\omega)]}(q_0 r) \\
&-\sqrt{2\pi}Rw_0 \sum_{n=1}^{N} \frac{\mu_n \cos[\mu_n(z+h)]}{q_n[\sin(2\mu_n h)+2\mu_n h]} \cdot \\
&\frac{\operatorname{sgn}(\omega)\cdot\left(e^{-i\omega\tau}-1\right)}{\omega} \cdot J_1(q_n R) H_0^{[1.5+0.5\operatorname{sgn}(\omega)]}(q_n r) \\
&-\frac{4Rw_0 i}{\sqrt{2\pi}} \sum_{n=N+1}^{\infty} \frac{\mu_n \cos[\mu_n(z+h)]}{q_n[\sin(2\mu_n h)+2\mu_n h]} \cdot \\
&\frac{e^{-i\omega\tau}-1}{\omega} \cdot I_1(q_n R) K_0(q_n r).
\end{aligned} \tag{B23}$$

Finally, the inverse Fourier transform is applied to obtain the potential field in inner and outer regions, as given in (11a) and (11b):

$$\Phi(r,z,t) = \frac{1}{\sqrt{2\pi}} \int_{-\infty}^{\infty} \tilde{\Phi}(r,z,\omega) e^{i\omega t} d\omega. \tag{B24}$$

Note that for each mode $n = 1, \ldots, \infty$, the threshold frequency ω_{sn} separates between propagating and evanescent modes, and is given by

$$\omega_{sn} = \frac{2\pi}{T_{sn}} = \frac{\pi c}{2h} \cdot (2n-1). \tag{B25}$$

APPENDIX C: CPU TIME

1. Technical information

- All calculations for the above examples were carried out on Windows 7, 64-bit operating system running on a Dual Core, Quad Thread 64bit Intel i3-2100 processor running at 3.10 HGz per core, and 3MB smart Cache machine.
- For the circular and the general shape disturbance models, Matlab R2007b software package 7.5.0.342 was used.

2. Measurements

Most of the examples in this study are based on 2 elementary calculation time-increments, such that for a constant observation point r, a time series is calculated from $t_{\min}$ to $t_{\max}$, using constant Δt time step, usually taken as $\Delta t = 1$ min for Tsunami wave and $\Delta t = 1$ s for Acoustic-Gravity waves. These elementary calculation time-increments are

- dt_1 - Tsunami wave of a circular disturbance, calculated with Quadrature numerical integration method. The measured elapsed real-time for a single time step was $dt_1 \approx 0.035$ s (averaged over 6000 time-steps).
- dt_2 - 10 modes of Acoustic-Gravity waves of a circular disturbance, calculated with Stationary-Phase approximation. The measured elapsed real-time for a single time step was $dt_2 \approx 0.001$ s (averaged over 6000 time-steps).

Hence, the general calculation times for a fixed distance r from a circular disturbance are

- Tsunami wave: $dt_1 \cdot (t_{\max} - t_{\min})/\Delta t$,
- Acoustic-Gravity wave: $dt_2 \cdot (t_{\max} - t_{\min})/\Delta t$.

For the rectangular disturbance, the application of the Green function method determines that the CPU time depends also on the spatial size of the disturbance and m, the number of elements, where each element is calculated according to the basic estimations above. Therefore, the calculation times for a fixed distance from a rectangular disturbance are

- Tsunami wave: $m \cdot dt_1 \cdot (t_{\max} - t_{\min})/\Delta t$,
- 10 modes of Acoustic-Gravity waves: $m \cdot dt_2 \cdot (t_{\max} - t_{\min})/\Delta t$.

[1] M. A. Nosov, "Tsunami generation in a compressible ocean," Phys. Chem. Earth B **24**, 437–441 (1999).
[2] M. A. Nosov, "Tsunami generation in a compressible ocean by vertical bottom motions," Izv., Acad. Sci., USSR, Atmos. Oceanic Phys. **36**(5), 661–669 (2000).
[3] M. A. Nosov and S. M. Skachko, "Nonlinear tsunami generation mechanism," Nat. Hazards Earth Syst. Sci. **1**, 251–253 (2001).
[4] M. A. Nosov, S. V. Kolesov, A. V. Ostroukhova, A. B. Alekseev, and B. W. Levin, "Elastic oscillations of the water layer in Tsunami source," Doklady Earth Sci. **404**(7), 1097–1100 (2005).
[5] M. A. Nosov and S. V. Kolesov, "Elastic oscillations of water column in 2003 Tokachi-oki tsunami source: in-situ measurements and 3-D numerical modeling," Nat. Hazards Earth Syst. Sci. **7**, 243–249 (2007).
[6] H. Miyoshi, "Generation of the tsunami in compressible water (Part I)," J. Oceanogr. Soc. Jpn. **10**, 1–9 (1954).
[7] C. C. L. Sells, "The effect of a sudden change in shape of the bottom of a slightly compressible ocean," Philos. Trans. R. Soc. London, Ser. A **1092**, 495–528 (1965).
[8] T. Yamamoto, "Gravity waves and acoustic waves generated by submarine earthquakes," Soil Dyn. Earthquake Eng. **1**, 75–82 (1982).
[9] M. Stiassnie, "Tsunamis and acoustic-gravity waves from underwater earthquakes," J. Eng. Math **67**, 23–32 (2010).
[10] G. Hendin, "Tsunami and acoustic-gravity waves in water of constant depth," Ph.D. thesis (Technion, Israel Institute of Technology, 2013), p. 121.
[11] G. F. Carrier, M. Krook, and C. E. Pearson, *Functions of a Complex Variable, Theory and Technique* (McGraw-Hill, New-York, 1966), p. 438.
[12] J. Tobias and M. Stiassnie, "An idealized model for tsunami," J. Geophys. Res. **116**, C06026, doi:10.1029/2010JC006763 (2011).
[13] N. W. McLachlan, *Theory and Application of Mathieu Functions* (Dover Publications, Inc., New York, 1964), p. 401.
[14] P. Moon and D. E. Spencer, *Field Theory Handbook* (Springer-Verlag, London, 1961), p. 236.